Understanding the Polypharmacological Profiles of Triple Reuptake Inhibitors by Molecular Simulation

Gao Tu, Tingting Fu, Fengyuan Yang, Jingyi Yang, Zhao Zhang, Xiaojun Yao, Weiwei Xue,* and Feng Zhu*

Cite This: https://doi.org/10.1021/acschemneuro.1c00127

Read Online

ACCESS | Metrics & More | Article Recommendations | Supporting Information

ABSTRACT: The triple reuptake inhibitors (TRIs) class is a class of effective inhibitors of human monoamine transporters (hMATs), which includes dopamine, norepinephrine, and serotonin transporters (hDATs, hNETs, and hSERTs). Due to the high degree of structural homology of the binding sites of those transporters, it is a great challenge to design potent TRIs with fine-tuned binding profiles. The molecular determinants responsible for the binding selectivity of TRIs to hDATs, hNETs, and hSERTs remain elusive. In this study, the solved X-ray crystallographic structure of hSERT in complex with escitalopram was used as a basis for modeling nine complexes of three representative TRIs (SEP225289, NS2359, and EB1020) bound to their corresponding targets. Molecular dynamics (MD) and effective post-trajectory analysis were performed to estimate the drug binding free energies and characterize the selective profiles of each TRI to hMATs. The common binding mode of studied TRIs to hMATs was revealed by hierarchical clustering analysis of the per-residue energy. Furthermore, the combined protein−ligand interaction fingerprint and residue energy contribution analysis indicated that several conserved and nonconserved "Warm Spots" such as S149, V328, and M427 in hDAT, F317, F323, and V325 in hNET and F335, F341, and V343 in hSERT were responsible for the TRI-binding selectivity. These findings provided important information for rational design of a single drug with better polypharmacological profiles through modulating multiple targets.

KEYWORDS: Polypharmacology, inhibition ratio, monoamine transporters, antidepressants, molecular simulation, multitarget drug design
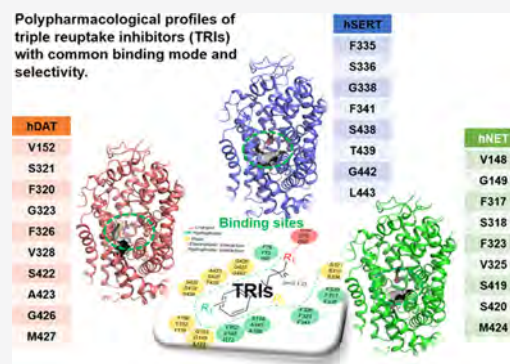
INTRODUCTION

Polypharmacology including multitarget drugs and combination therapies have been developed to achieve a more therapeutic effect for complex diseases such as psychiatric disorders, cancer, infections, and so on.[1] The tailorability of multitarget drugs in modulating the relevant pathways of complex diseases[2] is of critical importance for minimizing drug resistance issues, mitigating the adverse events of drug−drug interactions, and improving medication adherence among patients.[3,4] In recent years, the value of drugs against multiple targets is increasingly recognized by pharmaceutical research as their greater efficacy,[5−8] while designing a multitarget drug with fine-tuned properties in modulating two or more targets remains a challenge for medicinal chemists in drug discovery.[9] In particular, the design becomes more challenging when the protein belongs to the same family, such as G-protein coupled receptors (GPCRs),[10,11] kinases,[12] and transporters,[13] which are the causative mechanisms and therapeutic targets to the diseases.[14−16]

Human monoamine transporters (hMATs), including the dopamine transporter (hDAT), norepinephrine transporter (hNET), and serotonin transporter (hSERT), are secondary active transporters that belong to the solute carrier 6 (SLC6) family.[17,18] hDAT, hNET, and hSERT share great homology, with more than 50% sequence identity overall, and more than 70% homology within the transmembrane (TM) domains (Figure S1). The three closely related transporters are responsible for regulating neurotransmission via the reuptake of dopamine (DA), norepinephrine (NE), and serotonin (5-HT) from the extra-neuronal regions.[19] Thus, hDAT, hNET, and hSERT have been pharmacological targets for several neuropsychiatric and neurodegenerative disorders caused by dysfunction of neurotransmitter homeostasis in the brain.[19−21]

For single- or dual-target antidepressants, it is estimated that, for more than 60% of patients who suffered from major depressive disorder (MDD), the antidepressants are inadequate to achieve a satisfactory therapeutic effect due to the low remission rate and delayed therapeutic onset.[22,23] Nevertheless, alternative novel therapies (listed in Table S1)
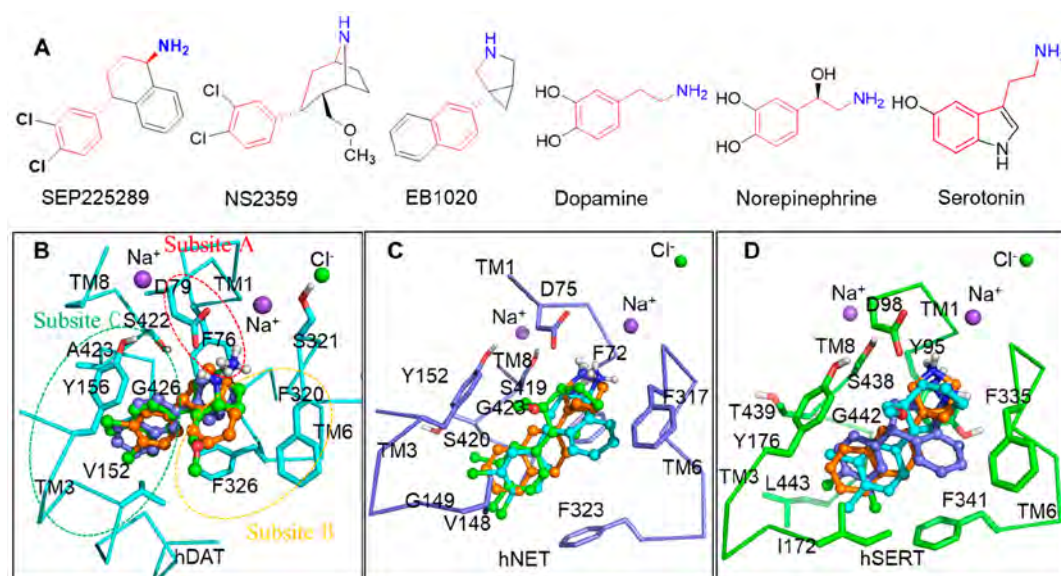
Figure 1. (A) Structures of the TRIs SEP225289, NS2359, and EB1020 as well as the substrates dopamine, norepinephrine, and serotine in this study. The scaffold of the structures were highlighted in red. (B) Superimposition of the docked poses of SEP225289 (orange), NS2359 (green), and EB1020 (blue) in the structure of hDAT (cyan stick). (C) Superimposition of the docked poses of SEP225289 (cyan), NS2359(green), and EB1020 (orange) in the structure of hNET (blue stick). (D) Superimposition of the docked poses of SEP225289 (blue), NS2359 (cyan), and EB1020 (orange) in the structure of hSERT (green stick). SEP225289, NS2359, and EB1020are represented by the ball and stick model. Locations of subsite A, subsite B, and subsite C are indicated by red, orange, and green dashed lines, respectively. Two Na+ and one Cl− ions are represented by the blue and green spheres, respectively.

from clinical trials revealed that simultaneously inhibiting the DA, NE, and 5-HT reuptake could rapidly increase the extracellular levels of neurotransmitter in different brain regions,[24] leading to better efficacy and safety and less tolerance against patients with MDD or other diseases such as attention deficit hyperactivity disorder, binge eating disorder, and cocaine addiction.[24−27]

Interestingly, the early design of TRIs were evolved from single or dual reuptake inhibitors of hMATs by simplifying the chemical structures,[28] which makes it so the scaffolds of the TRIs are very close to the native substrates DA, NE, or 5-HT (Figure 1A). Such a structural similarity has given rise to speculation that the central binding site of the transporters (Figure S1), which can be occupied by small molecules with different sizes (Figure 1A), have the strong ability of plasticity to function.[29] Herein, SEP225289, NS2359, and EB1020 were selected as the representative TRIs in current studies[25] by comprehensively considering the scaffold (substrate structure) similarity and substituent group diversity. The three TRIs exhibited excellent binding affinities against each protein of hMATs.[25] Importantly, the phase 2 or 3 clinical trials indicated that the polypharmacology profiles (for example the protein−ligand binding mode and the variation of drug inhibition ratio to different targets) may be responsible for their improved therapeutic effects.[25,26,30] However, there is a lack of understanding regarding the profiles of TRI polypharmacology pose restrictions on multitarget antidepressant development.[2,28,31,32]

In this study, to fill the aforementioned gap, a computational study was performed to predict the binding of SEP225289, NS2359, and EB1020 to the central site of hDAT, hNET, and hSERT at atomic levels. The structures of hDAT and hNET were constructed via homology modeling technique using the available X-ray crystal structure of hSERT in an outward-open conformation[33] as a template. The binding affinity of each TRI

to the corresponding target protein was estimated through molecular mechanics generalized Born surface area (MM/GBSA) method[34] based on the sampled binding modes derived from molecular dynamics (MD) simulation. Per-residue energy decomposition and molecular interaction fingerprint analysis provided important insights into the variation of the inhibition ratio that trigger differentiated treatment effects.[24,25]

RESULTS AND DISCUSSION

Docking Poses of TRIs at the Central Binding Site of hMATs. Like other classical antidepressants, such as escitalopram,[33] TRIs were developed as competitive inhibitors preventing the substrates (DA, NE, and 5-HT) from binding to hDAT, hNET, and hSERT.[25] To investigate the polypharmacology of TRIs as novel therapies at the atomic level, the complexes of SEP225289, NS2359, and EB1020 bound to their targets (Figure 1B−D) were predicted by docking them into the central binding sites of the highest quality structures of the three transporters in outward-open conformations so far. See details for the evolution of the modified hSERT crystal structure and hDAT and hNET homology models in the Supporting Information (Results and Discussion section).

Figure 1B−D displays the superimposed binding pose of each drug in the central binding site of the same target. The central binding site of hMATs is primarily surrounded by transmembrane (TM) helices 1, 3, 6, and 8 and can be further divided into three subsites (A, B, and C).[17] As shown, all the three drugs' positively charged nitrogen moieties occupied the regions of subsite A and form salt bridge interactions with the negatively charged side chains of the conserved aspartic acid in the targets (D79 in hDAT; D75 in hNET and D98 in hSERT), which plays a crucial role in ligand recognition.[18,22] In subsite B, the 1,2,3,4-tetrahydronapthalene of SEP225289, the

Table 1. Binding Affinities of the Studied Ligands from Calculation and Experiment (Energy in kcal/mol and IC$_{50}$ in nM)

| drug	target	ΔE_{ele}	ΔE_{VDW}	ΔG_{GB}	ΔG_{GBSUR}	ΔG_{CAL}[a]	ΔG_{exp}[b]	IC$_{50}$[c]
NS2359	hDAT	−70.51	−44.24	71.65	−5.01	−48.11	−11.34	10
	hNET	−55.57	−45.57	56.63	−4.99	−49.11	−12.33	2
	hSERT	−22.01	−40.45	23.71	−4.66	−43.42	−11.34	10
SEP225289	hDAT	−84.33	−40.82	82.43	−4.94	−47.65	−12.33	2
	hNET	−55.76	−40.53	56.07	−4.85	−45.07	−11.90	4
	hSERT	−39.61	−37.96	38.26	−4.71	−44.03	−11.13	14
EB1020	hDAT	−87.08	−35.21	88.41	−4.27	−40.00	−10.51	38
	hNET	−52.44	−36.62	52.29	−4.11	−40.88	−11.65	6
	hSERT	−23.72	−35.51	26.94	−4.21	−36.50	−10.03	84

[a]Calculated binding free energy using MM/GBSA method[34] in this work. [b]Experimental binding free energy calculated using $\Delta G_{exp} = RTln(IC_{50})$. [c]IC$_{50}$ values were from the experimental literature.[25]

methoxymethyl of NS2359, and the [3, 3, 0] hexane of EB1020 moiety interacts with aromatic residues (F320 and F326 in hDAT; F317 and F323 in hNET; F335 and F341 in hSERT) of the TM3 domain via hydrophobic interactions. For subsite C, the phenyl group of the drugs was enclosed in a hydrophobic pocket formed by the side chains of residues in TM3 and TM8 (V152, Y156, S422, A423 in hDAT; V148, Y152, S419, S420 in hNET; I172, Y176, S438, T439, and L443 in hSERT). The results cover most of the interaction features in the cocrystallized structure of escitalopram-hSERT,[33] which verified the rationality of the docking poses. Meanwhile, there are obvious differences between the TRI-binding and substrate-binding modes in three transporters by docking due to the headgroup of positive nitrogen of DA, NE, and 5-HT, which are far away from the TM6 in comparison with TRIs bound to hDAT, hNET, and hSERT, respectively, and the three substrates occupy the central binding site in three hMAT structures with a chemical space smaller than the regions of subsite B in TRI-binding complexes from the docking model (Figure S6). In addition, Figure 1B−D shows the ability of the hDAT, hNET, and hSERT central binding site to accommodate drugs with varying size; however, the plasticity of the pocket was not fully considered in the docking calculation.[35] In this regard, further MD simulation is necessary to characterize the structural dynamic behavior of the obtained nine binding complexes.[35−37]

Conformational Sampling of the TRI-Binding Complexes. Starting from the docking poses, unbiased MD simulations of the complexes in explicit solvent sampled the protein−ligand conformations, and all systems basically achieved convergence after 50 ns of simulations (Figure S7). To monitor the conformational states of the TRI-binding complexes, two pairs of gating residues (Arg85-Asp476 and Tyr156-Phe320 of hDAT; Arg81-Phe473 and Tyr152-Phe317 of hNET; Arg104-Glu493 and Tyr176-Phe335 of hSERT) in the external gate were picked out to calculate the distances between α carbon atoms of gating residues of three hMATs along each MD trajectory. Figure S8 shows that the TRIs binding in the central site of three hMATs primarily favor an outward-open conformation during MD simulations. The backbone atoms of the whole proteins are accompanied by an average value of ∼3.0 Å RMSD fluctuation with respect to the docked poses in all simulation systems. In comparison, the heavy atoms of a ligand in each system and the backbone atoms of residues around the ligand binding site gave an RMSD fluctuation from the initial structure of ∼0.5 and ∼1 Å, respectively. To get an overall view of the binding mode before and after MD simulations, the representative snapshots of
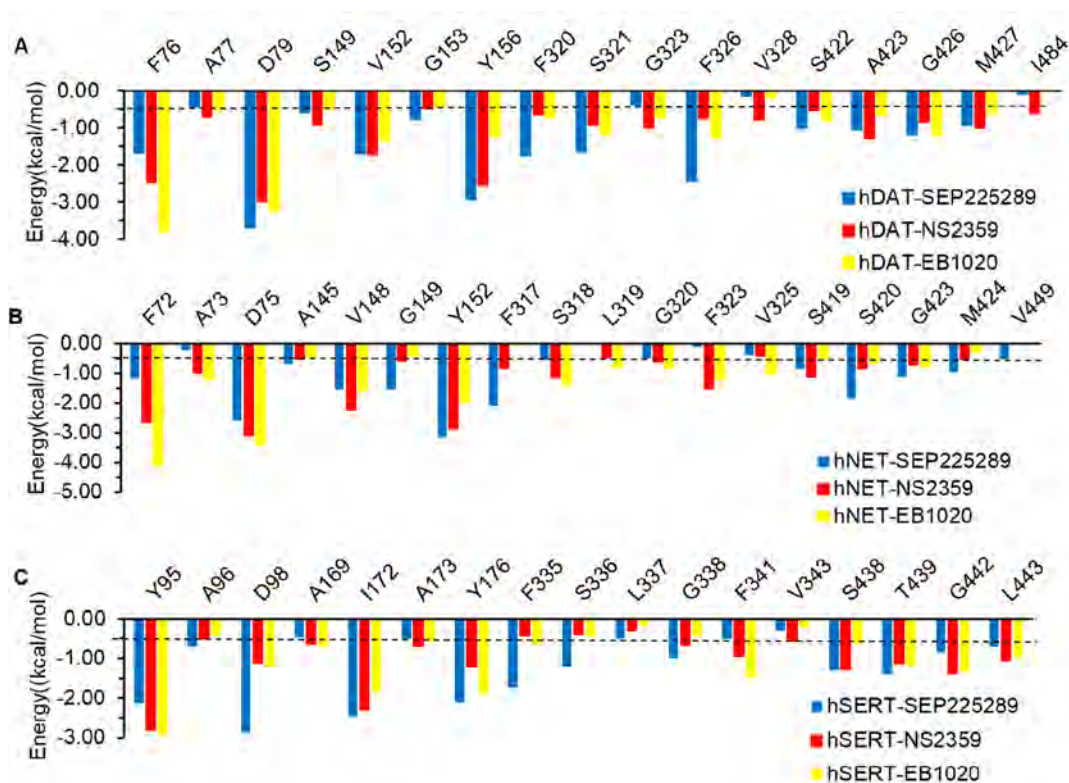
SEP225289, NS2359, and EB1020 binding to hDAT, hNET, and hSERT derived from equilibrated trajectories were superimposed onto the corresponding initial docking conformations (Figure S9). The details of the protein−ligand interaction features from MD simulations were analyzed in the following section. Figure S9 indicated that, in addition to the most well-preserved key interactions such as the salt bridge, there are some structural rearrangements by adjusting the orientation of the active site residues' side chain. For example, the flip of the residues F320, F326, V152, S422, and M427 in hDAT; F317, L319, F323, and S419 in hNET; and F335, F341, T431, and S438 in hSERT were found during the simulations. These results are consistent with the conclusion that MD simulations are essential for assessing and corroborating the predicted binding modes from docking calculations.[38]

Binding Free Energy of TRIs to Multiple Targets. The reliability of the predicted binding modes by MD simulations can be further judged by comparing the calculated binding free energies (ΔG_{CAL}) with experimental values (ΔG_{exp}).[39] Table 1 lists the results of ΔG_{CAL} and the details of the energy terms estimated by the MM/GBSA method[34] together with ΔG_{exp} and experimental IC$_{50}$.[25] The values of ΔG_{CAL} were in the range −49.11 kcal/mol (NS2359-hNET) to −36.50 kcal/mol (EB1020-hSERT). The correlation coefficient between the calculation and experiment was 0.84 (Figure 2). These values underline the reliability of the simulations.[40] As shown in Table 1, the major contributors to the nine binding complexes
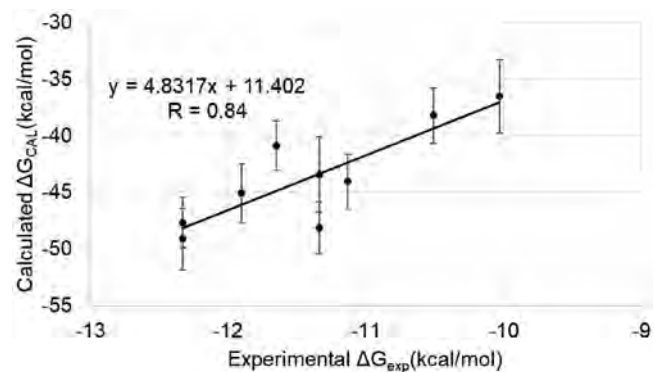
Figure 2. Comparison between the experimental and calculated binding affinities from the computational simulation using the data listed in Table 1. The correlation coefficient between the values of ΔG_{CAL} and ΔG_{exp} is 0.84. The calculated binding energy error bars represent the standard error.

Figure 3. Per-residue energy profiles for SEP225289, NS2359, and EB1020 binding in hDAT, hNET, and hSERT. For the nine simulated systems, the central site residues with a favorite energy contribution of more than 0.50 kcal/mol are displayed. The black dotted lines represent the cut off of −0.50 kcal/mol.

were the electrostatic energy (ΔE_{ELE}) and the van der Waals energy (ΔE_{VDW}) terms, whereas the polar solvation energy (ΔG_{GB}) was unfavorable for the interactions. Therefore, it could be concluded that the optimization of van der Waals and electrostatic interactions may improve the inhibitor binding affinities.

Tables S2−S4 list the per-residue energies for the nine complexes. According to previous studies of the similar system,[41,42] the binding free energy was dominated primary by the "Hot Spots" (per-residue absolute energy contribution value ≥ 1.5 kcal/mol) and "Warm Spots" (0.5 kcal/mol ≤ absolute energy contribution value < 1.5 kcal/mol) residues. Therefore, the energy contribution of −0.50 kcal/mol was used as a cut off, and the 17, 18, and 17 favorable contributors were characterized as important ones in the central binding sites of hDAT (Figure 3A), hNET (Figure 3B), and hSERT (Figure 3C), respectively. Figure 4 displays the molecular interactions between each TRI and the corresponding identified residues. The detailed descriptions of the binding modes can be found in the Supporting Information (Results and Discussion section). Among the characterized important residues, there were several "Hot Spots" (with favorite contributions more than −2.00 kcal/mol) identified in the binding sites; for example, D79 in hDAT contributes −3.68, −2.99, and −3.25 kcal/mol for SEP225289, NS2359, and EB1020 recognition (Table S2), respectively. F72 was one of the largest contributors (−4.10 kcal/mol) in the hNET−EB1020 complex (Table S3), and D98 in hSERT contributed more binding energy for SEP225289 (−2.89 kcal/mol) than for NS2359 (1.12 kcal/mol) and EB1020 (−1.20 kcal/mol) (Table S4). In addition, there are some "Warm Spots" (with favorite contributions from −0.50 to −2.00 kcal/mol) which were

identified in the central binding sites interacting with different substituted moieties of the inhibitors. Previous studies have shown that "Warm Spots" play important roles in regulating the behaviors of ligands binding to protein subtypes,[42] which will be further discussed in the next section.

Understanding the Polypharmacology of TRIs. *Profiling the Common Binding Mode of TRIs.* To understand the polypharmacology mechanism of TRIs, it is essential to profile the common binding mode of TRIs. Based on the data of per-residue energy, hierarchical cluster analysis was performed to get an overview of the energy profiles of each residue in the binding sites contributing to different drugs binding to their corresponding targets (Figure 5). The drugs analyzed include two single-target inhibitors[42] (Escitalopram and Talopram), one dual-target inhibitor[42] (Ligand 10), and four triple reuptake inhibitors (Amitifadine,[22] SEP225289, NS2359, and EB1020), which have different binding affinities to hDAT, hNET, or hSERT.

As shown in Figure 5, a total of 48 residues in the central binding site of the three target proteins were mainly clustered into categories A, B, and C. From the columns of the heatmap, the clustering result shows that the 12 residues in cluster A and B contributed much more than the other to the binding of all the drugs. Furthermore, the contribution of the residues in categories A and B demonstrated that their interactions with TRIs are weaker compared with that of the single- and dual-target bound complexes; this is because of the relatively small size of the TRI chemical structure. However, from the rows of the heatmap, except for EB1020-hNET and Escitalopram-hNET, all of the single- and dual-target drug bound complexes are mainly clustered into group I. Meanwhile, all of the TRI bound complexes were clustered into group II.
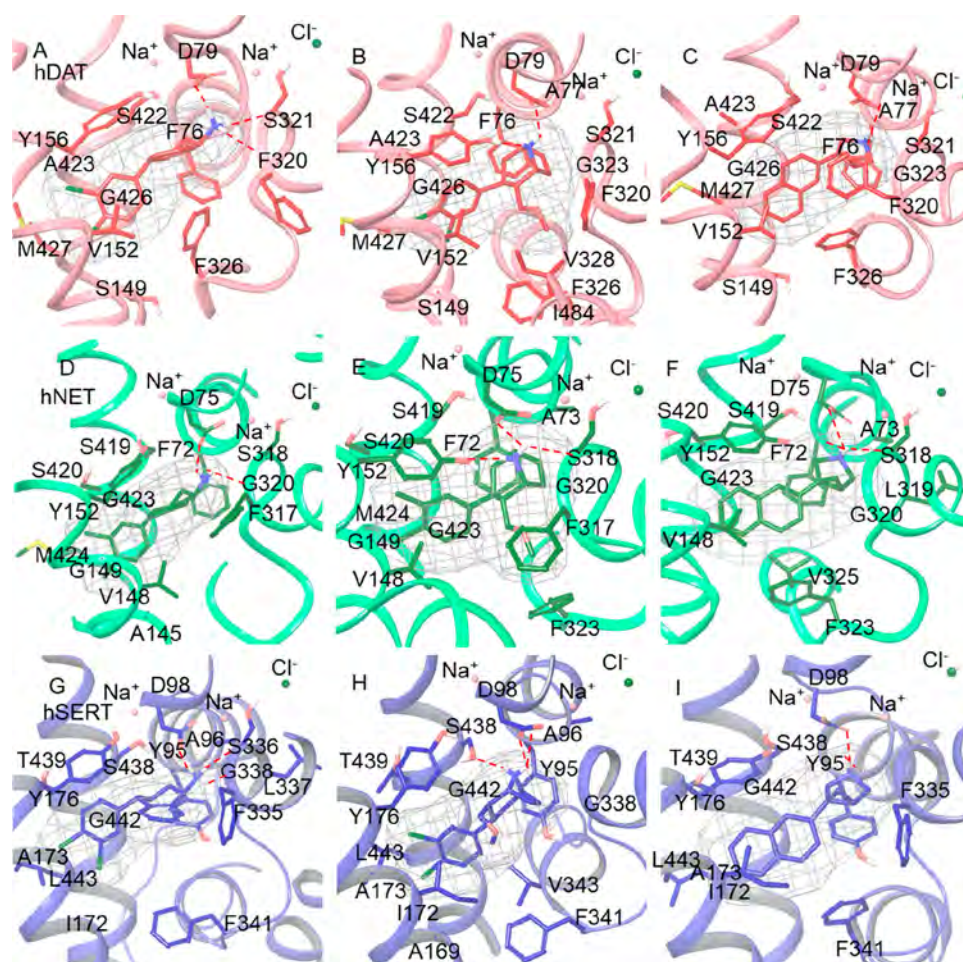
Figure 4. Binding modes of the studied TRIs in the central site of targets derived from MD simulations. The ligands in the binding site are shown as sticks and mesh. Proteins hDAT, hNET, and hSERT are represented in pink, green, and blue cartoons, respectively. (A−C) The ligands (red) SEP225289, NS2359, and EB1020 in the hDAT binding site. (D−F) The ligands (dark green) NS2359, EB1020, and SEP225289 in the hNET binding site. (G−I) The ligands (dark blue) NS2359, EB1020, and SEP225289 in the hSERT binding site. Two Na+ ions and one Cl− ion are represented by the pink and blue spheres, respectively.

Inspired by the figures shown in clustering analysis (Figure 5) and interaction modes (Figure 4), the common binding mode of EB1020, SEP225289, and NS2359 in the central binding sites of hDAT, hNET, and hSERT was profiled in Figure 6. As shown, the amine group of TRIs (R_1) engaged in hydrogen interaction or electrostatic interaction with conserved aspartic acid (D79 in hDAT, D75 in hNET, and D98 in hSERT). The phenyl moiety of TRIs (R_3) extends into the hydrophobic pocket shaped by TM3 and TM8 residues S149, V152, Y156, S422, A423, and G426 in hDAT; A145, V148, Y152, S419, S420, and G423 in hNET; and Y95, A169, I172, Y176, S438, T439, and G442 in hSERT. In addition, the R_2 substituent also established hydrophobic interactions with the side chains of F320, S321, and F326 in hDAT; F317, S318, and F323 in hNET; and S336, F335, and F341 in hSERT. Moreover, the protein−ligand pharmacophore models of the nine representative structures illustrated that hydrophobic interactions and hydrogen bond interactions are the predominant features for the three target proteins (Figure 7). In addition, there are some distinctive features which are also found here; for example, in the hDAT bound complex, the aromatic amino acid Y156 formed one π−π interaction, one CH−π interaction, and one T-shaped interaction with SEP225289, NS2359, and EB1020, respectively (Figure 7A−

C). In hNET bound complexes, the side chain of Y152 formed hydrogen bonds with NS239 and EB1020, respectively. (Figure 7D−F). In hSERT bound complexes, one CH−π interaction was formed with SEP225289. The three drugs' positively charged nitrogen moiety mainly participated in hydrogen bonding in TM1 and TM6 regions (Figure 7G−I). The pharmacophore models of the nine simulated complexes were consistent with the identified common binding features in the central binding site for TRIs. The profiles of the common binding mode and protein−ligand pharmacophore not only suggested that electric and hydrophilic interactions are the main thermodynamic driving forces for the formation of TRI binding complexes, which also provided useful information for the design or optimization of TRI analogues with improved selectivity.

Identifying the Interaction Features Underlying TRI Inhibitory Ratios. It is well-known that the stabilization of a ligand binding to its target protein is through the conformation-dependent recognition mechanism,[43] which means that structural changes of the protein or ligand can lead to the variation of their binding affinities. On the basis of this concept, it would become feasible to further decipher the molecular mechanism of the TRI inhibitory ratio to the different targets using the obtained binding mode of the
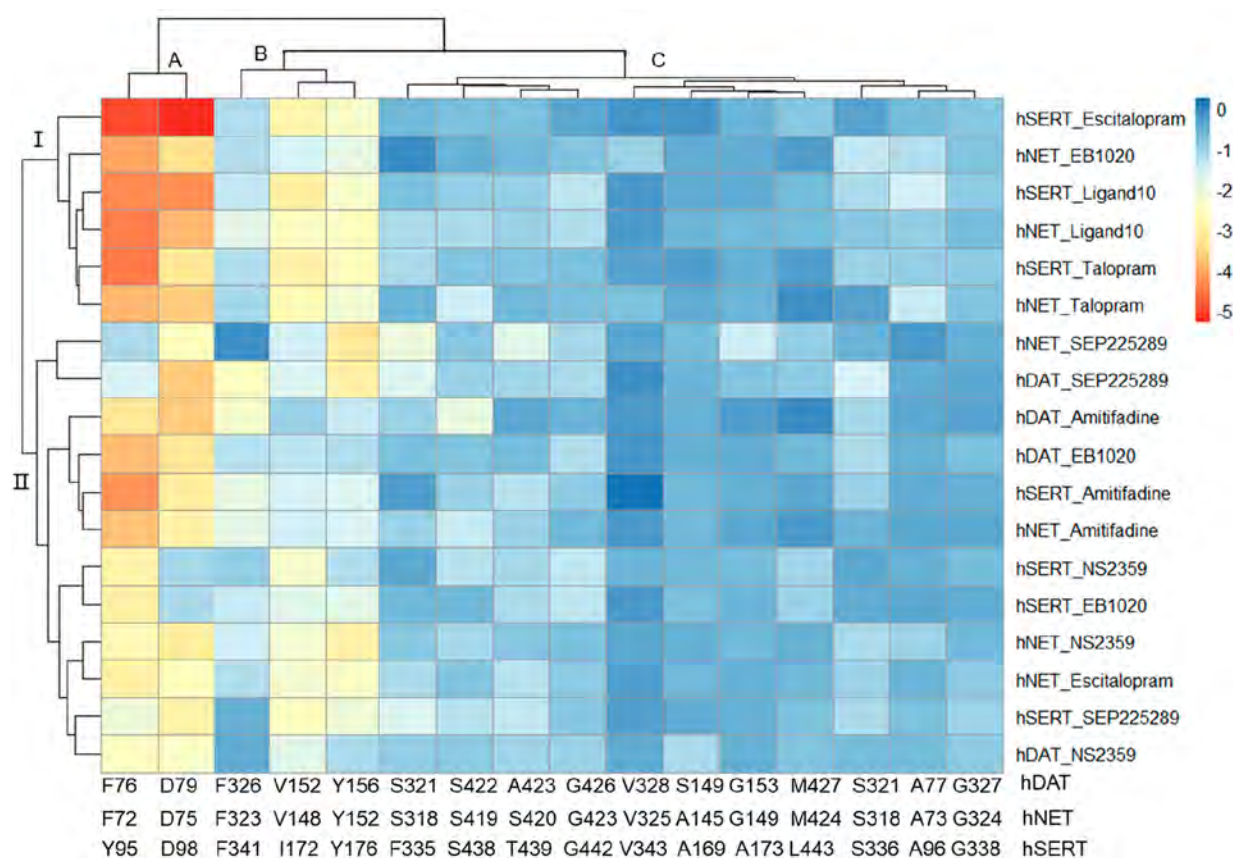
Figure 5. Hierarchical clustering and heatmap analysis of per-residue energy contribution for ligands binding to hDAT, hNET, or hSERT. The ligands include two single-target inhibitors (escitalopram, talopram), one dual-target inhibitor (Ligand 10), and four triple reuptake inhibitors (amitifadine, NS2359, EB1020, and SEP225289). Rows represent the 18 protein−ligand complexes, and columns represent the 15 residues in the central binding site.

binding complexes. Thus, the interaction features that determine the relative binding affinities of TRIs to hDAT, hNET, and hSERT were identified by comparisons of the modes of interaction.

Comparison of the Interactions of Specific TRIs among hDAT, hNET, and hSERT. The superimposition for each drug in the central sites of hDAT, hNET, and hSERT indicated the conformational varieties of both conserved and nonconserved residues (Figure 8A−C). To quantitatively determine those differences, the molecular fingerprint of interactions which was calculated with more than 50% probability interactions was depicted in Figure 8D−F. The details of the protein−ligand interaction types were listed in Tables S5−S7. Although the interactions between F76 (hDAT) and F72 (hNET) with SEP225289 and between D98 (hSERT) with NS2359 and EB1020 are weaker than those of other complexes (Figure 5), the two conserved residues (D79 and Y156 in hDAT, D75 and Y152 in hNET, and D98 and Y176 in hSERT) and the one nonconserved residue (F76 in hDAT, F72 in hNET, and Y95 in hSERT) are mainly responsible for the drug recognition in the binding sites and interact with the three TRIs in a similar way (Figure 8).

In addition, several residues located in the equivalent positions of TM3, TM6, and TM8 domains of the multiple binding sites which form unique interactions with the drugs were identified. For SEP225289, the unique interaction residues are V152, G153, S321, F326, S422, and M427 in hDAT; V148, G149, S318, F323, S419, M424, and V449 in hNET; and A173, I172, S336, F341, S438, and L443 in hSERT (Figure 3 and Figure 8D). For example, the phenyl group of SEP225289 mainly embedded into the TM3 and TM8 regions, and the nonconserved "Warm Spot" residues (V152, G153, and M427 in hDAT; V148, G149, and M424 in hNET; and I172, A173, and L443 in hSERT) have significant difference conformations (Figure 8A). The TM6a region in hDAT and hSERT was found to be located closer to the nitrogen group of SEP225289 based on the superposition-based methods, and per-residue energy decomposition results further suggested that there are stronger hydrogen bond interactions between the "Warm Spots" (S321 in hDAT, S336 in hSERT) and the positively charged nitrogen of SEP225289 as compared to "Warm Spot" S318 in hNET. Meanwhile, the residue F326 in hDAT undergoes significant structural rearrangements for a favorable conformation during the MD simulation, which form a stronger interaction with the 1,2,3,4-tetrahydronaphthalene moiety of SEP225289 with respect to the ligand bound to F323 in hNET and F341 in hSERT. The phenyl moiety of SEP225289 bound to hNET stays closer to the TM3 and TM8 regions (G149 and M424), compared to the ligand bound to hDAT (G153 and M427) and hSERT (A173 and L443). Furthermore, compared to the "Warm Spots" V152 in hDAT and V148 in the hNET bound complex, the per-residue energy contribution of the residue I172 has the higher contribution to the binding of SEP225289 to hSERT. By comparison of the interactions of SEP225289 binding to hDAT, hNET, and hSERT, these results suggest that there is the central binding
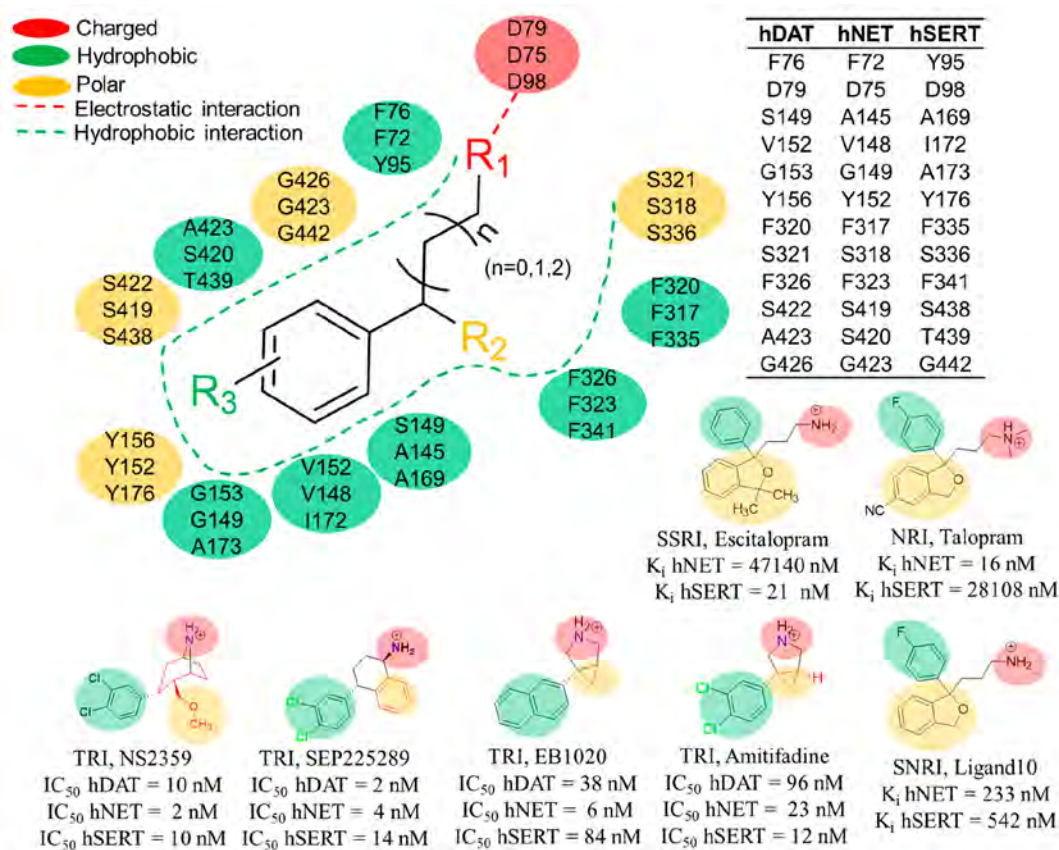
Figure 6. Analysis of TRIs in the presence of a common scaffold (black). The three major substituents R$_1$, R$_2$, and R$_3$ working as a pharmacophore were highlighted in red, orange, and green, respectively. The residues possess the same spatial position in the binding sites of hDAT, hNET, and hSERT and directly interact with the pharmacophores of TRIs, which were labeled in the same color.

site "Warm Spots" within hMAT domains that exhibit unique interactions, which plays an important part in determining the SEP225289 inhibitor selectivity.

Figure 8E shown that residues V152, S321, F326, V328, S422, G426, M427, and I484 in hDAT; V148, S318, F323, V325, S419, G423, and M424 in hNET; and I172, S336, G338, F341, V343, S438, G442, and L443 in hSERT form unique interactions with NS2359. In three NS2359 bound complexes, the tropane moiety of NS2359 undergoes a large conformational change relative to its initial structure (Figure S9). Compared to hSERT-NS2359, the nitrogen group of NS2359 is slightly closer to the TM6a region and forms additional hydrogen bond interactions with "Warm Spots" S336 in hDAT and S318 in hNET, respectively. Meanwhile, the methoxymethyl group of NS2359 extends into the TM6 region, forming hydrogen bond interactions with the conserved "Warm Spots" F326, F323, and F341 corresponding to hDAT, hNET, and hSERT, respectively, and the interaction energy for residue F323 is higher than that of residues F326 in hDAT and F341 in hSERT. In addition, we also found that the interactions of NS2359 and residues (S438, G442, and L443) in hSERT are subtly higher than those of residues (S422, G426 and M427) in hDAT and those of residues (S419, G423 and M424) in hNET (Figure 3 and Figure 8B), while the residue S438 in hSERT forms hydrogen interactions with SEP225289.

The residues identified to form unique interactions with EB1020 are V152, F320, S321, V328, A423, G426, and M427 in hDAT; V148, F317, S318, V325, S420, G423, and M424 in hNET; and I172, F335, S336, V343, T439, G442, and L443 in

hSERT (Figure 8F). The positively charged nitrogen of EB1020 participated in two or three hydrogen bond interactions with TM1 and TM6 regions, where the interaction of the "Warm Spots" S336 in hSERT and the group is weaker in the per-residue energy contribution than the corresponding residue S321 in the hDAT bound complex and S318 in the hNET bound complex. Similarly, the 3-azabicyclo[3,1,0] hexane group of EB1020 contacts with TM6 regions, and the per-residue interaction energies of the "Warm Spots" F317 in hSERT are significantly lower than those of the corresponding "Warm Spots" F320 in hDAT and F335 in hNET. By comparing with the representative snapshots of hDAT-EB1020 and hNET-EB1020, we also found that the tail naphthyl group of EB1020 in hSERT moves closer to the TM8 region than to the EB1020−hDAT and EB1020−hNET complexes (Figure 3 and Figure 8C) and, thus, makes relatively stronger hydrophobic interactions with several "Warm Spots" (M424, T439, and L443 in hSERT).

Moreover, those residues were also found to respond to the structural modifications of TRIs to improve their potency and selectivity toward hDAT, hNET, and hSERT. NS2359 belongs to the NeurSearch series,[44] in which the tropane moiety was maintained as a cocaine scaffold (Figure 9B). As shown, the modifications of the R$_1$ position with a methyl (−CH$_3$) group or hydrogen atoms (−H) at the periphery have a minor influence on the binding affinity to hDAT, hNET, and hSERT. However, the substituents at R$_2$ in tropane analogues not only slightly tweak the inhibition ratio but also reduce side effects, which afforded these analogues with a lower abuse potential.[44]
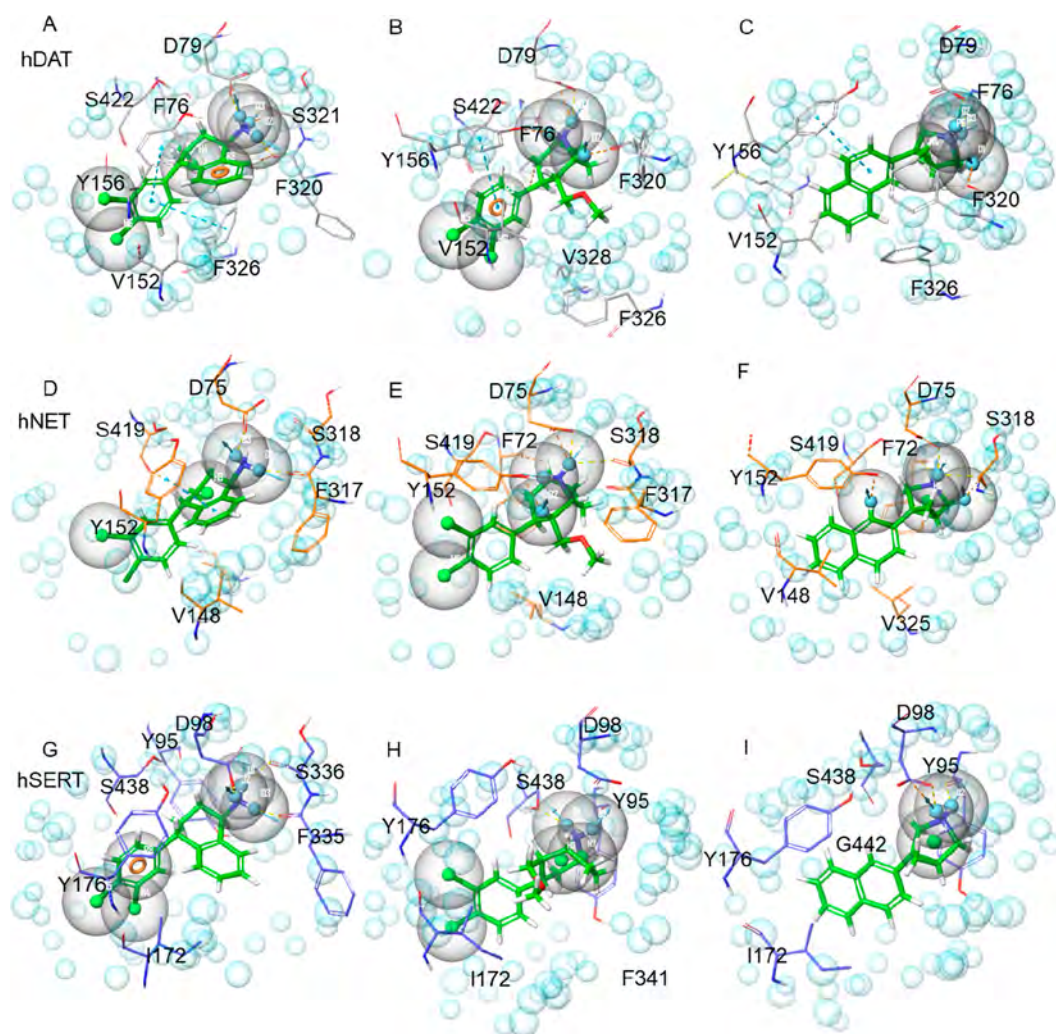
Figure 7. Pharmacophore models of SEP225289, NS2359, and EB1020 with hDAT(A−C), hNET (D−F), and hSERT (G−I), respectively. The ligands in the binding site are shown as green sticks. The cyan spheres mean the excluded volume shell.

As a member of the 4-aryl-1,2,3,4-tetrahydronaphthalene series, SEP225289 originates from cis-sertraline (Figure 9A). The potency of SEP225289 to hDAT and hNET was significantly enhanced when the core R_1 position of cis-sertraline was substituted by an amino (−NH$_2$) group. Therefore, it could be concluded that the selectivity could be drastically altered with different R_1 groups, and the amino group at R_1 plays a crucial role for the binding affinities to hDAT and hNET. Compared to SEP225289, the other ligands' activities to hDAT, hNET, and hSERT were decreased when an N-methyl or an amino group is placed in the R_2 or R_3 position.

EB1020 was derived from the 1-aryl-3-azabicyclo[3,1,0] hexane series by modifying the aryl ring to improve the binding affinities (Figure 9C).[45,46] Compared with the structure and pharmacological profiles of bicifadine, the 3,4-dichlorophenyl or 2-naphthyl groups at the R_2 position are aromatic substituents, and the substituents at R_1 are mainly groups of hydrogen atoms or methyls.

Comparison of the Interactions of Each Target with SEP225289, NS2359, and EB1020. For TRIs-hDAT complexes, according to the calculated per-residue energy (Table S5), 15 residues (F76, D79, I148, S149, V152, Y156, F320, F326, V328, S422, A423, M427, V430, A480, and I484) mainly

participated in three types of interactions including ionic (salt bridge), hydrogen bond, and hydrophobic contacts (Figure 10D). For example, the "Hot Spot" F76 engaged in the hydrophobic interaction with EB1020 and NS2359 (Figure 10A,D), and the calculated energies were −3.81 and −2.47 kcal/mol (Figure 3A and Table S2), respectively. Moreover, the "Warm Spots" in hDAT have a distinct difference in their interactions with EB1020, SEP225289, and NS2359. For example, the interactions between four "Warm Spots" (S149, V152, Y156, F326, and A423) with NS2359 and SEP225289 were preserved better than that of EB1020, mainly due to the molecular size (R_2 substituent) of NS2359 and SEP225289, which are larger than the cyclopropyl ring of EB1020.

In the central binding site of hNET, the tetrahydronaphthalene moiety of SEP225289 interacts with the aromatic residues Y152 and F317 through π−π and hydrophobic interactions (Table S6) with the corresponding energies of −3.16 and −2.08 kcal/mol (Figure 3B), respectively. Likewise, the methoxymethyl group of NS3259 forms an important hydrophobic interaction with residues F317 and F323 (Table S6 and Figure 3B). In addition, the tropane moiety of NS2359 undergoes a significant rotation relative to its initial docking pose due to the hindrance of Y152 (hNET), whose aromatic side chain group causes a shift of the ester group toward Y152
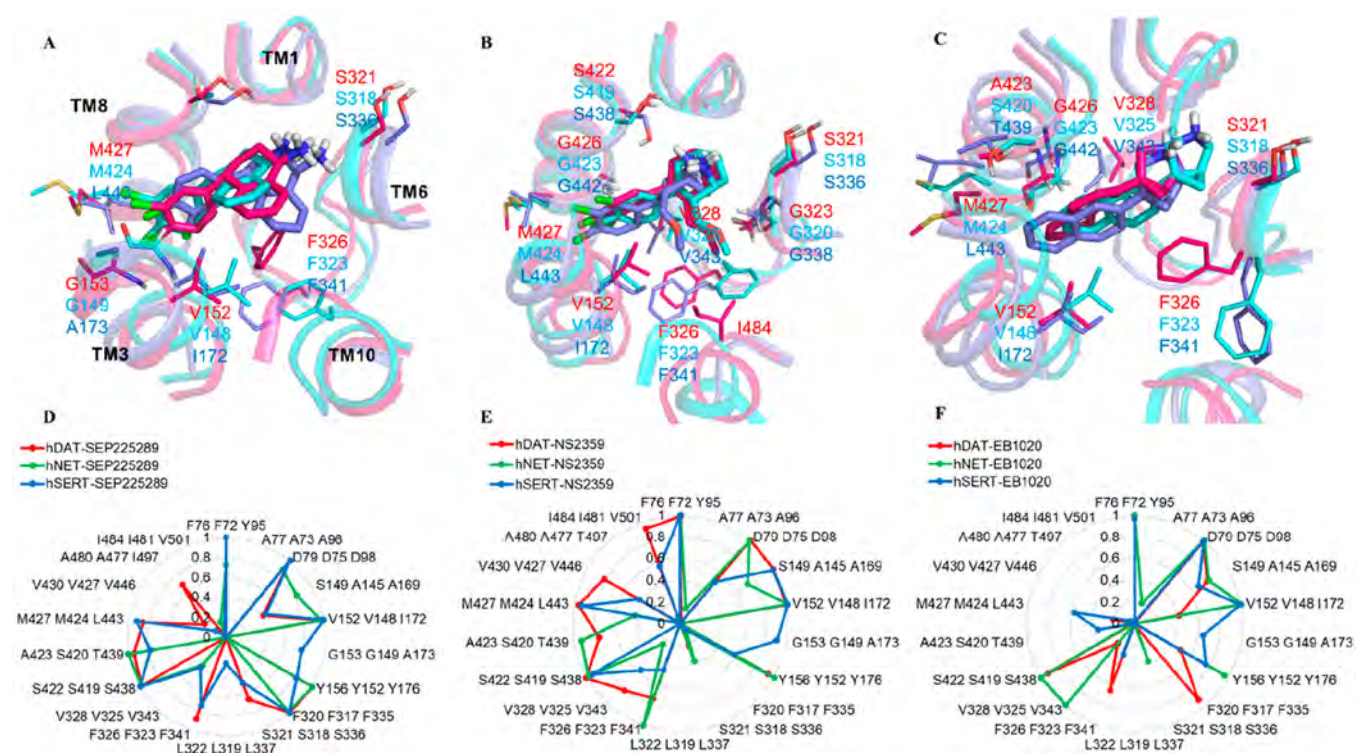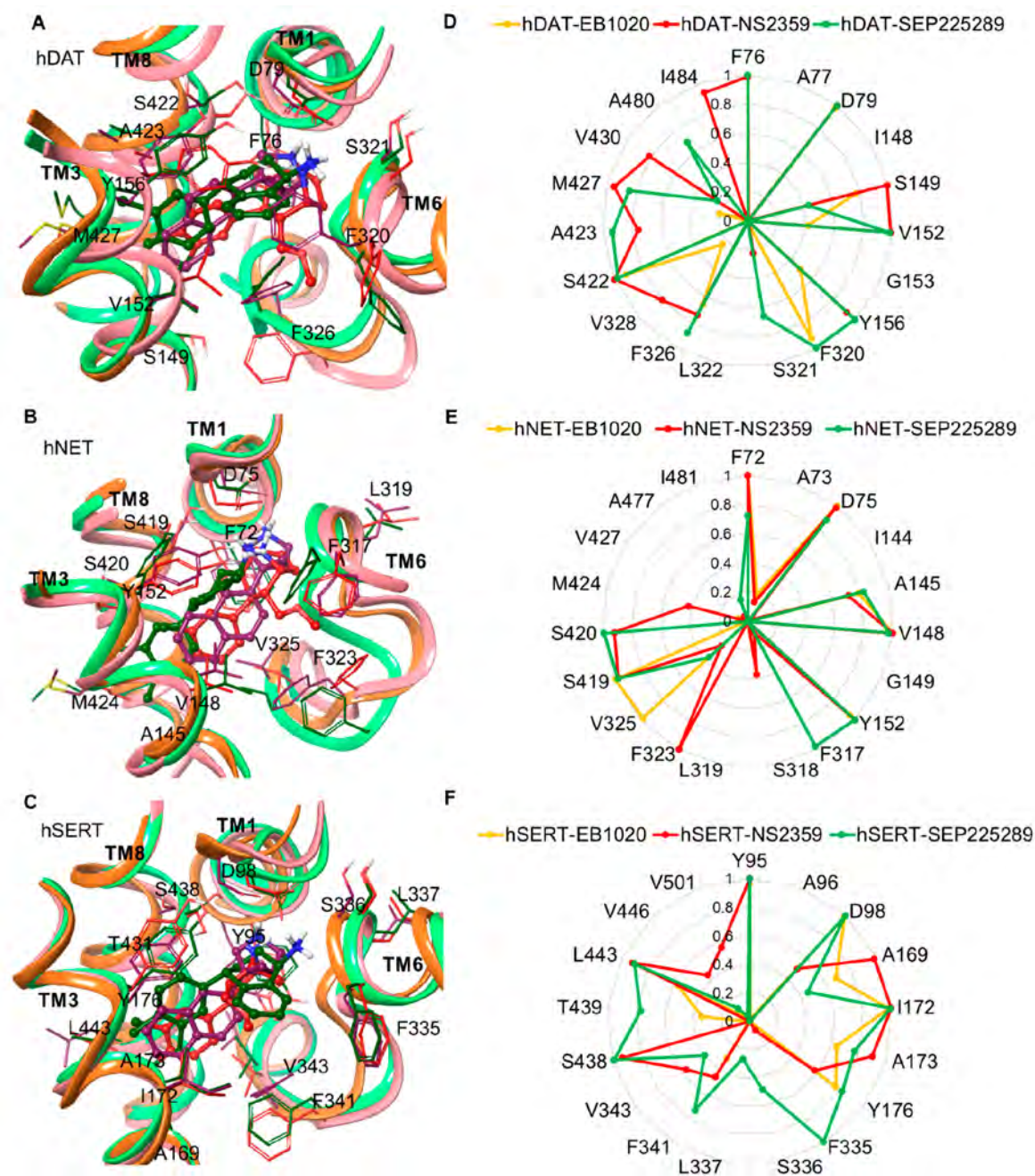
Figure 8. Comparison of the structural complexes of the same drug such as (A) SEP225289, (B) NS2359, and (C) EB1020 binding to hDAT (red), hNET (green), and hSERT (blue). The protein structures are represented as a cartoon with the "Warm Spots" shown as lines. The ligands are as displayed as sticks. (D−F) The molecular fingerprint with more than 50% probability interactions between proteins and ligands.
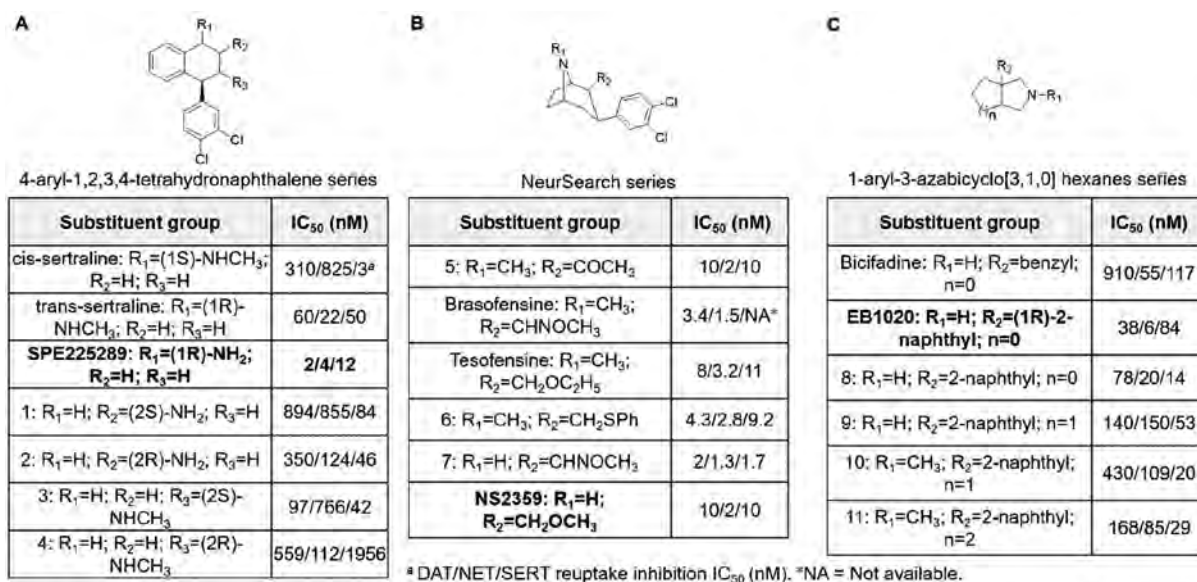
Figure 9. SAR analysis of the three series TRIs with three representative drugs (SEP225289, NS2359, and EB1020) studied in this work. (A) Chemical structures of 4-aryl-1,2,3,4-tetrahydronaphthalene series. (B) Chemical structures of selected NeurSearch series. (C) Chemical structures of 1-aryl-3-azabicyclo[3,1,0] hexane series.

(Figure S9). Compared with SEP225289 and NS2359, the nitrogen group of EB-1020 moves toward TM1 regions including residues F72 and D75 (Figure 10E). In particular, F72 contributes −4.10 kcal/mol to EB1020 binding (Figure 3B), indicating that the important scaffold of EB-1020 (azabicyclo[3.1.0]hexane) plays a significant role in the binding affinity. In addition, four "Warm Spots" (F317, V325, S420, and F323) show a distinct difference in their frequency of interaction with EB1020, SEP225289, and NS2359. For SEP225289, residues F317 and S420 form a more stable interaction than that of the NS2359 and EB1020. On the contrary, the EB1020 interaction with V325 and the NS2359 interaction with F323 form more stable hydrophobic interactions than the SEP225289, because the aromatic rings in EB1020 and NS2359 are closer to the TM6 region (Figure 10B).

Figure 10. Comparison of the structural complexes of different drugs SEP225289 (green), NS2359 (red), and EB1020 (maroon) binding to the same target such as (A) hDAT, (B) hNET, and (C) hSERT. The protein structures are represented as a cartoon with the binding site residues shown as lines. The ligands are displayed as a ball-and-stick model. (D−F) The molecular fingerprint between proteins and ligands. The numbers 0−1 in the radar chart indicate the probability of interactions between the ligands and a certain residue based on 500 snapshots from the last 50 ns equilibrated trajectories.

As for hSERT bound complexes, the naphthyl group of EB1020 forms hydrophobic interactions with F341 and F335. However, stronger contacts were found for the corresponding methoxymethyl group of NS2359 with G338, F341, and V343 and for the tetrahydronapthalene group of SEP225289 with S336, L337, G338, and F335 (Figure 10C and Figure 3C). Combined with the per-residue energy result, the molecular interaction fingerprint analysis revealed that the interactions between three "Warm Spots" (A169, V343, and V501) and NS2359 were stronger than that of EB1020 and SEP225289. Compared with NS2359 and EB1020, SEP225289 forms more

stable interactions with another three "Warm Spots" (F335, F341, and T439) (Figure 10F and Figure 3C).

In addition, superimposition of the conformations from docking from the MD simulation showed that ligands binding to hDAT and hNET undergo relatively large conformational changes, and the porcupine plot analysis implied that the plasticity of the binding pocket in two target proteins is more flexible (Figures S9 and S10).

The combined binding modes and structure activity relationship (SAR) analysis clearly showed that the residues, which form unique interactions with a ligand, play a key role in

regulating the binding affinity. Interestingly, the per-residue energy hierarchical clustering analysis (Figure 5) demonstrated that all of them belong to the "Warm Spots". Therefore, the observed selectivity of TRIs to hDAT, hNET, and hSERT is primarily due to the specific role of conserved and non-conserved residues distributed on TM3, TM6, and TM8 domains of the binding sites.

CONCLUSION

The present study employs a combined computational approach to understand the binding modes and selectivity underlying the polypharmacology of TRIs. Results show that EB1020, SEP225289, and NS2359 share a common binding mode in the central binding sites of hDAT, hNET, and hSERT. The estimated binding free energies indicated that the contributions from the hydrophobic interaction and electric primary dominate the binding affinities of TRIs to their targets. The identified 10 "Warm Spots" (V152, S321, F320, G323, F326, V328, S422, A423, G426, and M427) in hDAT, 9 "Warm Spots" (V148, G149, F317, S318, F323, V325, S419, S420, and M424) in hNET, and 8 "Warm Spots" (F335, S336, G338, F341, S438, T439, G442, and L443) in hSERT located in TM3, TM6, and TM8 domains of the multiple binding sites have a pronounced effect on the inhibitors' selectivity. The results in this study provided useful information for understanding the polypharmacological profiles of TRIs to hDAT, hNET, and hSERT, which are important to the rational design of new TRIs for better therapeutics.

MATERIALS AND METHODS

Preparation of Ligand and Protein Structures. The 3D structures of the studied TRIs (SEP225289, NS2359, and EB1020) were obtained from PubChem[47] with the corresponding CIDs 9947999, 11408320, and 16095349. The ligands were then minimized by the *LigPrep*[48] with the *OPLS3* force field[49] to generate the low energy conformations, and the ionized state was realized by *Epik*[50] at a pH value of 7.0 ± 2.0 for docking.

The sequences of hNET and hDAT were taken from UniPort (Entries: P23975 and Q01959), and the crystal structure of the hSERT mutant (Y110A-I291A-T439S) was taken from the Protein Data Bank (PDB code: 5I71[33]). To generate the native structure of hSERT, the Protein Mutation and Modification tool in Schrödinger[51] was used to mutate the three mutations back in 5I71,[33] and the modified structure was preprocessed by the Protein Preparation Wizard tool in Schrödinger[51] with the OPLS3 force field.[52] The homology models of hDAT and hNET were built by MODELLER[53] using the native structure of hSERT as a template (Figure S5A). The sequence alignment was performed by ClustalW2[54] and visualized by ESPript3[55] (Figure S1). The cocrystallized escitalopram and two functional Na+ in hSERT were manually fitted into the ion binding sites of hNET and hDAT through the align module in PyMOL[56] to generate the escitalopram−hDAT and escitalopram−hNET complexes (Figure S5).

Ligand Docking. The Glide[57] standard precision (SP) mode was chosen for molecular docking. The docking grid box for hDAT, hNET, and hSERT were defined by centering on the escitalopram as reference in bound complexes using the Receptor Grid Generation in Glide.[57] The reasonable docked poses of SEP225289, NS2359, and EB1020 binding in hDAT, hNET, and hSERT were selected according to the orientation of escitalopram in the complex structures as well as the interactions, which are essential for TRI binding.[22,42]

Simulation Systems Setups. The nine predicted complexes were obtained through docking and the PPM server[58] for determining the orientation of the membrane transporter. Then, the transmembrane segments were inserted into the explicit hydrated POPC membrane bilayer with ∼195 lipids, forming a periodic cell (95 Å × 95 Å × 118

Å) of each system, and of ions were added to neutralize the charges of the system in approximately 0.15 M NaCl (containing ∼55 Na+ and ∼55 Cl− ions) by using the CHARMM-GUI Membrane Builder.[59] The TIP3P[60] water thickness of 20 Å was placed at the top and bottom of the protein with ∼19 668 water molecules, with the overall system containing ∼93 800 atoms (Table S8). We employed the program LEaP tool in AMBER16[61] to generate the topology and coordinate files for each simulated system. The parameters of protein and lipid were obtained by ff14SB and Lipid14,[62] respectively. The Joung/Cheathamion parameters were used to characterize the ion parameters. AMBER force field 2 (gaff2) parameter sets for the ligands and the partial charges were derived from RESP[63] calculation using an HF/6-31G* electrostatic potential calculated by Gaussian09.[64]

MD Simulation. GPU-accelerated AMBER16[61] was adopted for all MD simulations. The first energy minimization step was to apply a harmonic restraint on the lipid and the solute atom (force constant = 10 kcal mol−1 Å−2) and then to release all atoms to move freely in the second step. In each step, the entire system was minimized for 10 000 steps followed by an energy minimization of 5000 steps using the Steepest Descent algorithm and the conjugate gradient method. Subsequently, a two-step equilibration was performed, each system was heated from 0 K to approximately 100 K and then gradually to 310 K with the protein and lipid restrained over 100 ps in the NVT ensembles. Then, all the simulated complexes were repeated for 10 times unconstrained NPT dynamics (5 ns) at 310 K and 1 atm. Finally, the PMEMD were carried out for 100 ns MD production simulation durations in the NPT ensemble at 310 K and 1 atm using the periodic boundary condition. The temperature and pressure were maintained using a Langevin thermostat and a Monte Carlo barostat, respectively. Electrostatic interactions with a distance cutoff of 10 Å were calculated using particle mesh Ewald (PME) method.[65] The SHAKE algorithm[66] was used to keep all-bonds constraints, and the time step was set as 2.0 fs.

Thermodynamics Analysis. To investigate the thermodynamic properties of protein−ligand interactions, based on the system stability determined by the fluctuation of root-mean-square deviations (RMSDs), 500 snapshots were extracted from the last 50 ns of MD trajectories with a time interval of 100 ps. The binding free energy of ligands binding to hDAT, hNET, and hSERT were calculated by the MM/GBSA method[34] in accordance with the following equation:

$$\Delta G_{CAL} = \Delta E_{VDW} + \Delta E_{ELE} + \Delta G_{GB} + \Delta G_{GBSUR} \qquad (1)$$

where ΔG_{CAL} was obtained by summing van der Waals (ΔE_{VDW}) energies and the electrostatic (ΔE_{ELE}), the sum of polar (ΔG_{GB}), and nonpolar (ΔG_{GBSUR}) contributions, respectively. Snapshots (500) extracted from the last 50 ns trajectory along the MD trajectory were used for energy calculations. The per-residue energy contribution between the ligands and proteins was calculated with the following equation:

$$\Delta G_{CAL}^{per-residue} = \Delta G_{VDW}^{per-residue} + \Delta G_{ELE}^{per-residue} + \Delta G_{GB}^{per-residue} + \Delta G_{GBSUR}^{per-residue} \qquad (2)$$

where $\Delta G_{VDW}^{per-residue}$, $\Delta G_{ELE}^{per-residue}$, and $\Delta G_{GB}^{per-residue}$ in eqn 2 are defined with the same meanings as those of the corresponding terms in eqn 1. The difference is that the nonpolar solvent energy ($\Delta G_{GBSUR}^{per-residue}$) is modeled by a recursive approximation of a sphere around an atom starting from an icosahedron (ICOSA).

Hierarchical Clustering Analysis. The clustering heatmap of 288 residues with individual residue energy contribution (0.00−4.10 kcal/mol) to ligands binding in proteins was constructed by the pheatmap package in R.[67] Then, the data are clustered in a two-way display of a data matrix in which the individual cells are displayed as colored rectangles by using the Euclidean distance function[68] across these predicted systems; then, the hierarchical tree graphs were directly output. The complete-linkage hierarchical clustering is applied to define the distance between two clusters before merging. The Euclidean distance was selected to calculate similarity levels among vectors

$$\text{Distance}\,(a,\,b) = \sum_i |a_i - b_i|$$

where i represents each dimension of per-residue energies a and b. The corresponding gradient of color sets the highest value of residue energy contribution in the heatmap to bright red; the lowest one was set to fade gradually to dark blue.

Intermolecular Interaction Fingerprints Analysis. Snapshots (500) were extracted from the final 50 ns equilibrium MD run, and the use of protein–ligand interaction fingerprint (IFP) analysis was applied using IChem software.[69] For each frame, the calculation zones of the complex were defined as the regions within 5 Å of the ligand mass center. During the calculation, seven important pharmacological properties (including hydrophobic, aromatic, H-bond donor, H-bond acceptor, positively ionizable, negatively ionizable, and meta) of the atoms of proteins and ligands were evaluated by parsing atoms and bond connectivity fields. In this analysis, the calculated protein–ligand interaction fingerprints between frames of molecular dynamics simulations were displayed via radar charts. If a particular interaction between receptor and ligand was detected, "1" was the output; otherwise, "0" was recorded. Finally, the calculated results were displayed in a radar chart to clearly represent the ligand–receptor interactions.

Pharmacophore Modeling. The 3D pharmacophore model of TRI binding in hMATs was built on the Maestro module of Schrodinger.[70] First, the nine representative structures were obtained from the final 50 ns MD trajectories. Second, the receptor–ligand workspace pharmacophore of each complex was used to generate key chemical features by manually inspecting the protein–ligand interaction, whose features are important for binding. Then, the receptor-based excluded volume with a scaling factor of 0.50 for van der Waals atom radii was added. Finally, the pharmacophore of each TRI-binding complex generated the chemical features with the hydrogen bonds, hydrophobic interactions, and excluded volume shell.

■ ASSOCIATED CONTENT

ⓢ Supporting Information

The Supporting Information is available free of charge at https://pubs.acs.org/doi/10.1021/acschemneuro.1c00127.

List of triple reuptake inhibitors (TRIs) entered into clinical trials; per-residue energy of residues; fingerprints of molecular interaction between three hMATs and three studied TRIs; summary of nine complexes for MD simulations; sequence alignment of hSERT, hNET, and hDAT; MolProbity Ramachandran analysis of the modeled three hMAT structures; cartoon representation of the modified hSERT (blue), the modeled hNET (cyan), and hDAT (warm pink); docking poses; RMSD of the nine simulated complexes; distances between α carbon atoms of gating residues; structural superimposition between the poses of three TRIs; and porcupine plots (PDF)

■ AUTHOR INFORMATION

Corresponding Authors

Weiwei Xue − *School of Pharmaceutical Sciences, Chongqing Key Laboratory of Natural Product Synthesis and Drug Research, Chongqing University, Chongqing 401331, China; Central Nervous System Drug Key Laboratory of Sichuan Province, Luzhou 646106, China;* ⓞ orcid.org/0000-0002-3285-0574; Email: xueww@cqu.edu.cn

Feng Zhu − *School of Pharmaceutical Sciences, Chongqing Key Laboratory of Natural Product Synthesis and Drug Research, Chongqing University, Chongqing 401331, China; College of Pharmaceutical Sciences, Zhejiang University, Hangzhou 310058, China;* ⓞ orcid.org/0000-0001-8069-0053; Email: zhufeng@zju.edu.cn

Authors

Gao Tu − *School of Pharmaceutical Sciences, Chongqing Key Laboratory of Natural Product Synthesis and Drug Research, Chongqing University, Chongqing 401331, China*

Tingting Fu − *School of Pharmaceutical Sciences, Chongqing Key Laboratory of Natural Product Synthesis and Drug Research, Chongqing University, Chongqing 401331, China; College of Pharmaceutical Sciences, Zhejiang University, Hangzhou 310058, China*

Fengyuan Yang − *School of Pharmaceutical Sciences, Chongqing Key Laboratory of Natural Product Synthesis and Drug Research, Chongqing University, Chongqing 401331, China; College of Pharmaceutical Sciences, Zhejiang University, Hangzhou 310058, China*

Jingyi Yang − *School of Pharmaceutical Sciences, Chongqing Key Laboratory of Natural Product Synthesis and Drug Research, Chongqing University, Chongqing 401331, China*

Zhao Zhang − *School of Pharmaceutical Sciences, Chongqing Key Laboratory of Natural Product Synthesis and Drug Research, Chongqing University, Chongqing 401331, China*

Xiaojun Yao − *State Key Laboratory of Applied Organic Chemistry and Department of Chemistry, Lanzhou University, Lanzhou 730000, China;* ⓞ orcid.org/0000-0002-8974-0173

Complete contact information is available at:
https://pubs.acs.org/10.1021/acschemneuro.1c00127

Author Contributions

W.X. and F.Z. designed the experiments. G.T. performed computational simulations. G.T., T.F., F.Y., J.Y., Z.Z., X.Y., W.X., and F.Z. analyzed the data. G.T., W.X., and F.Z. wrote the paper. All authors approved the final version of the manuscript.

Notes

The authors declare no competing financial interest.

■ ABBREVIATIONS

TRIs, triple reuptake inhibitors; hMATs, human monoamine transporters; hDAT, human dopamine hNET, human norepinephrine transporter; hSERT, human serotonin transporter; MD, molecular dynamics; MDD, major depressive disorder; MM/GBSA, molecular mechanics generalized born surface area; IFPs, interaction fingerprints analysis; TM, transmembrane domains; SAR, structure activity relationship

■ REFERENCES

(1) Bolognesi, M. L., and Cavalli, A. (2016) Multitarget Drug Discovery and Polypharmacology. *ChemMedChem* 11, 1190−1192.

(2) Ramsay, R. R., Popovic-Nikolic, M. R., Nikolic, K., Uliassi, E., and Bolognesi, M. L. (2018) A perspective on multi-target drug discovery and design for complex diseases. *Clinical and translational medicine* 7, 3.

(3) Talevi, A. (2015) Multi-target pharmacology: possibilities and limitations of the "skeleton key approach" from a medicinal chemist perspective. *Front. Pharmacol. 6*, 205.

(4) Sikazwe, D. (2012) The multi-target drug design era is here, consider it. *Drug Des.: Open Access 1*, 1000−1001.

(5) Chaudhari, R., Tan, Z., Huang, B., and Zhang, S. (2017) Computational polypharmacology: a new paradigm for drug discovery. *Expert Opin. Drug Discovery 12*, 279−291.

(6) Fathima, A. J., Murugaboopathi, G., and Selvam, P. (2018) Pharmacophore Mapping of Ligand Based Virtual Screening, Molecular Docking and Molecular Dynamic Simulation Studies for Finding Potent NS2B/NS3 Protease Inhibitors as Potential Anti-dengue Drug Compounds. *Curr. Bioinf. 13*, 606−616.

(7) Chen, J., Wang, J., Yin, B., Pang, L., Wang, W., and Zhu, W. (2019) Molecular Mechanism of Binding Selectivity of Inhibitors toward BACE1 and BACE2 Revealed by Multiple Short Molecular Dynamics Simulations and Free-Energy Predictions. *ACS Chem. Neurosci. 10*, 4303−4318.

(8) Chen, J., Yin, B., Wang, W., and Sun, H. (2020) Effects of Disulfide Bonds on Binding of Inhibitors to beta-Amyloid Cleaving Enzyme 1 Decoded by Multiple Replica Accelerated Molecular Dynamics Simulations. *ACS Chem. Neurosci. 11*, 1811−1826.

(9) Anighoro, A., Bajorath, J., and Rastelli, G. (2014) Poly-pharmacology: challenges and opportunities in drug discovery. *J. Med. Chem. 57*, 7874−7887.

(10) Hauser, A. S., Attwood, M. M., Rask-Andersen, M., Schioth, H. B., and Gloriam, D. E. (2017) Trends in GPCR drug discovery: new agents, targets and indications. *Nat. Rev. Drug Discovery 16*, 829−842.

(11) Sokouti, B., Rezvan, F., and Dastmalchi, S. (2017) GPCRTOP v.1.0: One-Step Web Server for Both Predicting Helical Trans-membrane Segments and Identifying G Protein-Coupled Receptors. *Curr. Bioinf. 12*, 80−84.

(12) Li, Y. H., Wang, P. P., Li, X. X., Yu, C. Y., Yang, H., Zhou, J., Xue, W. W., Tan, J., and Zhu, F. (2016) The Human Kinome Targeted by FDA Approved Multi-Target Drugs and Combination Products: A Comparative Study from the Drug-Target Interaction Network Perspective. *PLoS One 11*, No. e0165737.

(13) Lin, L., Yee, S. W., Kim, R. B., and Giacomini, K. M. (2015) SLC transporters as therapeutic targets: emerging opportunities. *Nat. Rev. Drug Discovery 14*, 543−560.

(14) Wang, Y., Zhang, S., Li, F., Zhou, Y., Zhang, Y., Wang, Z., Zhang, R., Zhu, J., Ren, Y., Tan, Y., et al. (2019) Therapeutic target database 2020: enriched resource for facilitating research and early development of targeted therapeutics. *Nucleic Acids Res. 48*, D1031−D1041.

(15) Avram, S., Halip, L., Curpan, R., and Oprea, T. I. (2020) Novel drug targets in 2019. *Nat. Rev. Drug Discovery 19*, 300.

(16) Khan, A., Zahra, A., Mumtaz, S., Fatmi, M. Q., and Khan, M. J. (2020) Integrated In-silico Analysis to Study the Role of microRNAs in the Detection of Chronic Kidney Diseases. *Curr. Bioinf. 15*, 144−154.

(17) Kristensen, A. S., Andersen, J., Jorgensen, T. N., Sorensen, L., Eriksen, J., Loland, C. J., Stromgaard, K., and Gether, U. (2011) SLC6 neurotransmitter transporters: structure, function, and regulation. *Pharmacol. Rev. 63*, 585−640.

(18) Navratna, V., and Gouaux, E. (2019) Insights into the mechanism and pharmacology of neurotransmitter sodium symport-ers. *Curr. Opin. Struct. Biol. 54*, 161−170.

(19) Cheng, M. H., and Bahar, I. (2019) Monoamine transporters: structure, intrinsic dynamics and allosteric regulation. *Nat. Struct. Mol. Biol. 26*, 545−556.

(20) Xue, W., Fu, T., Zheng, G., Tu, G., Zhang, Y., Yang, F., Tao, L., Yao, L., and Zhu, F. (2020) Recent Advances and Challenges of the Drugs Acting on Monoamine Transporters. *Curr. Med. Chem. 27*, 3830−3876.

(21) Srivastava, N., Mishra, B. N., and Srivastava, P. (2019) In-Silico Identification of Drug Lead Molecule Against Pesticide Exposed-neurodevelopmental Disorders Through Network-based Computa-tional Model Approach. *Curr. Bioinf. 14*, 460−467.

(22) Xue, W., Wang, P., Tu, G., Yang, F., Zheng, G., Li, X., Li, X., Chen, Y., Yao, X., and Zhu, F. (2018) Computational identification of the binding mechanism of a triple reuptake inhibitor amitifadine for the treatment of major depressive disorder. *Phys. Chem. Chem. Phys. 20*, 6606−6616.

(23) Xue, W., Yang, F., Wang, P., Zheng, G., Chen, Y., Yao, X., and Zhu, F. (2018) What Contributes to Serotonin-Norepinephrine Reuptake Inhibitors' Dual-Targeting Mechanism? The Key Role of Transmembrane Domain 6 in Human Serotonin and Norepinephrine Transporters Revealed by Molecular Dynamics Simulation. *ACS Chem. Neurosci. 9*, 1128−1140.

(24) Lane, R. M. (2015) Antidepressant drug development: Focus on triple monoamine reuptake inhibition. *J. Psychopharmacol. 29*, 526−544.

(25) Subbaiah, M. A. M. (2018) Triple Reuptake Inhibitors as Potential Therapeutics for Depression and Other Disorders: Design Paradigm and Developmental Challenges. *J. Med. Chem. 61*, 2133−2165.

(26) Sharma, H., Santra, S., and Dutta, A. (2015) Triple reuptake inhibitors as potential next-generation antidepressants: a new hope? *Future Med. Chem. 7*, 2385−2406.

(27) Skolnick, P. (2012) Triple-Uptake Inhibitors (Broad-Spectrum Antidepressants). *Polypharm. Drug Discovery*, 363−382.

(28) Marks, D. M., Pae, C. U., and Patkar, A. A. (2008) Triple reuptake inhibitors: the next generation of antidepressants. *Curr. Neuropharmacol. 6*, 338−343.

(29) Wang, K. H., Penmatsa, A., and Gouaux, E. (2015) Neurotransmitter and psychostimulant recognition by the dopamine transporter. *Nature 521*, 322−327.

(30) Richelson, E. (2013) Multi-modality: a new approach for the treatment of major depressive disorder. *Int. J. Neuropsychopharmacol. 16*, 1433−1442.

(31) Li, P., Wang, J., Wang, X., Ding, Q., Bai, X., Zhang, Y., Su, D., Zhang, W., Zhang, W., and Tang, B. (2019) In situ visualization of ozone in the brains of mice with depression phenotypes by using a new near-infrared fluorescence probe. *Chem. Sci. 10*, 2805−2810.

(32) Margret, A. A., and Arumugam, G. K. (2018) A Therapeutic Paradigm to Appraise the Competence of Chitosan Oligosaccharide Lactate Targeting Monoamine Oxidase-A and P-Glycoprotein to Contest Depression by Channeling the Blood Brain Barrier. *Curr. Bioinf. 13*, 273−279.

(33) Coleman, J. A., Green, E. M., and Gouaux, E. (2016) X-ray structures and mechanism of the human serotonin transporter. *Nature 532*, 334−339.

(34) Kollman, P. A., Massova, I., Reyes, C., Kuhn, B., Huo, S., Chong, L., Lee, M., Lee, T., Duan, Y., Wang, W., et al. (2000) Calculating structures and free energies of complex molecules: combining molecular mechanics and continuum models. *Acc. Chem. Res. 33*, 889−897.

(35) Durrant, J. D., and McCammon, J. A. (2011) Molecular dynamics simulations and drug discovery. *BMC Biol. 9*, 71.

(36) Liu, X., Shi, D., Zhou, S., Liu, H., Liu, H., and Yao, X. (2018) Molecular dynamics simulations and novel drug discovery. *Expert Opin. Drug Discovery 13*, 23−37.

(37) Guo, Y., Peng, Z., Liu, J., Yuan, N., Wang, Z., and Du, J. C. (2019) Systematic Comparisons of Positively Selected Genes between Gossypium arboreum and Gossypium raimondii Genomes. *Curr. Bioinf. 14*, 581−590.

(38) Zhao, H., and Caflisch, A. (2015) Molecular dynamics in drug design. *Eur. J. Med. Chem. 91*, 4−14.

(39) Kitamura, K., Tamura, Y., Ueki, T., Ogata, K., Noda, S., Himeno, R., and Chuman, H. (2014) Binding free-energy calculation is a powerful tool for drug optimization: calculation and measurement of binding free energy for 7-azaindole derivatives to glycogen synthase kinase-3beta. *J. Chem. Inf. Model. 54*, 1653−1660.

(40) Kenny, P. W. (2017) Comment on The Ecstasy and Agony of Assay Interference Compounds. *J. Chem. Inf. Model. 57*, 2640−2645.

(41) Fu, T. T., Tu, G., Ping, M., Zheng, G. X., Yang, F. Y., Yang, J. Y., Zhang, Y., Yao, X. J., Xue, W. W., and Zhu, F. (2020) Subtype-

selective mechanisms of negative allosteric modulators binding to group I metabotropic glutamate receptors. *Acta Pharmacol. Sin.*, 1 DOI: 10.1038/s41401-020-00541-z.

(42) Zheng, G., Yang, F., Fu, T., Tu, G., Chen, Y., Yao, X., Xue, W., and Zhu, F. (2018) Computational characterization of the selective inhibition of human norepinephrine and serotonin transporters by an escitalopram scaffold. *Phys. Chem. Chem. Phys.* 20, 29513–29527.

(43) Klebe, G. (2015) Protein-ligand interactions as the basis for drug action. In *Multifaceted Roles of Crystallography in Modern Drug Discovery*, pp 83–92, Springer.

(44) Chen, Z., Yang, J., and Skolnick, P. (2007) The Design, Synthesis and Structure–Activity Relationship of Mixed Serotonin, Norepinephrine and Dopamine Uptake Inhibitors. In *Transporters as Targets for Drugs*, pp 131–154, Springer.

(45) Micheli, F., Cavanni, P., Andreotti, D., Arban, R., Benedetti, R., Bertani, B., Bettati, M., Bettelini, L., Bonanomi, G., Braggio, S., et al. (2010) 6-(3,4-dichlorophenyl)-1-[(methyloxy)methyl]-3-azabicyclo-[4.1.0]heptane: a new potent and selective triple reuptake inhibitor. *J. Med. Chem.* 53, 4989–5001.

(46) Micheli, F., Cavanni, P., Arban, R., Benedetti, R., Bertani, B., Bettati, M., Bettelini, L., Bonanomi, G., Braggio, S., Checchia, A., et al. (2010) 1-(Aryl)-6-[alkoxyalkyl]-3-azabicyclo[3.1.0]hexanes and 6-(aryl)-6-[alkoxyalkyl]-3-azabicyclo[3.1.0]hexanes: a new series of potent and selective triple reuptake inhibitors. *J. Med. Chem.* 53, 2534–2551.

(47) Kim, S., Chen, J., Cheng, T., Gindulyte, A., He, J., He, S., Li, Q., Shoemaker, B. A., Thiessen, P. A., Yu, B., et al. (2019) PubChem 2019 update: improved access to chemical data. *Nucleic Acids Res.* 47, D1102–D1109.

(48) *LigPrep, Version 2.3*, Schrödinger, LLC: New York, NY, 2009.

(49) Price, D. J., and Brooks, C. L., 3rd. (2005) Detailed considerations for a balanced and broadly applicable force field: a study of substituted benzenes modeled with OPLS-AA. *J. Comput. Chem.* 26, 1529–1541.

(50) *Epik, Version 2.0*, Schrödinger, LLC: New York, NY, 2009.

(51) Release, S. (2018) 4: *BioLuminate*, Schrödinger, LLC, New York.

(52) Harder, E., Damm, W., Maple, J., Wu, C., Reboul, M., X iang, J. Y., Wang, L., Lupyan, D., Dahlgren, M. K., Knight, J. L., et al. (2016) OPLS3: A Force Field Providing Broad Coverage of Drug-like Small Molecules and Proteins. *J. Chem. Theory Comput.* 12, 281–296.

(53) Webb, B., and Sali, A. (2016) Comparative Protein Structure Modeling Using MODELLER. *Curr. Protoc. Protein Sci.* 86, 291–2937.

(54) Larkin, M. A., Blackshields, G., Brown, N. P., Chenna, R., McGettigan, P. A., McWilliam, H., Valentin, F., Wallace, I. M., Wilm, A., Lopez, R., Thompson, J. D., et al. (2007) Clustal W and Clustal X version 2.0. *Bioinformatics* 23, 2947–2948.

(55) Robert, X., and Gouet, P. (2014) Deciphering key features in protein structures with the new ENDscript server. *Nucleic Acids Res.* 42, W320–324.

(56) *PyMOL Molecular Graphics System, Version 1.3*, Schrödinger, LLC.

(57) *Glide, Version 5.5*, Schrödinger, LLC: New York, NY, 2009.

(58) Lomize, M. A., Pogozheva, I. D., Joo, H., Mosberg, H. I., and Lomize, A. L. (2012) OPM database and PPM web server: resources for positioning of proteins in membranes. *Nucleic Acids Res.* 40, D370–376.

(59) Wu, E. L., Cheng, X., Jo, S., Rui, H., Song, K. C., Davila-Contreras, E. M., Qi, Y., Lee, J., Monje-Galvan, V., Venable, R. M., et al. (2014) CHARMM-GUI Membrane Builder toward realistic biological membrane simulations. *J. Comput. Chem.* 35, 1997–2004.

(60) van der Spoel, D., and van Maaren, P. J. (2006) The Origin of Layer Structure Artifacts in Simulations of Liquid Water. *J. Chem. Theory Comput.* 2, 1–11.

(61) *AMBER, Version 16*, University of California: San Francisco, CA, 2016.

(62) Dickson, C. J., Madej, B. D., Skjevik, A. A., Betz, R. M., Teigen, K., Gould, I. R., and Walker, R. C. (2014) Lipid14: The Amber Lipid Force Field. *J. Chem. Theory Comput.* 10, 865–879.

(63) Wang, J., Wang, W., Kollman, P. A., and Case, D. A. (2006) Automatic atom type and bond type perception in molecular mechanical calculations. *J. Mol. Graphics Modell.* 25, 247–260.

(64) Frisch, M., Trucks, G., Schlegel, H., Scuseria, G., Robb, M., Cheeseman, J., Scalmani, G., Barone, V., Mennucci, B., and Petersson, G. (2009) *Gaussian 09*, Gaussian, Inc., Wallingford, CT.

(65) Petersen, H. G. (1995) Accuracy and efficiency of the particle mesh Ewald method. *J. Chem. Phys.* 103, 3668–3679.

(66) Springborg, M., and Kirtman, B. (2007) Efficient vector potential method for calculating electronic and nuclear response of infinite periodic systems to finite electric fields. *J. Chem. Phys.* 126, 104107.

(67) Tippmann, S. (2015) Programming tools: Adventures with R. *Nature* 517, 109–110.

(68) Hu, L. Y., Huang, M. W., Ke, S. W., and Tsai, C. F. (2016) The distance function effect on k-nearest neighbor classification for medical datasets. *SpringerPlus* 5, 1304.

(69) Da Silva, F., Desaphy, J., and Rognan, D. (2018) IChem: A Versatile Toolkit for Detecting, Comparing, and Predicting Protein-Ligand Interactions. *ChemMedChem* 13, 507–510.

(70) *Maestro, Version 9.0*, Schrödinger, LLC: New York, NY, 2009.